

## Pattern density function for reconstruction of three-dimensional porous media from a single two-dimensional image

Mingliang Gao,<sup>1,2</sup> Qizhi Teng,<sup>1,\*</sup> Xiaohai He,<sup>1</sup> Chen Zuo,<sup>1</sup> and Zhengji Li<sup>1</sup>

<sup>1</sup>College of Electronics and Information Engineering, Sichuan University, Chengdu 610065, China

<sup>2</sup>Northwest University for Nationalities, College of Electrical Engineering, Lanzhou 730030, China

(Received 9 September 2015; revised manuscript received 1 December 2015; published 22 January 2016)

Three-dimensional (3D) structures are useful for studying the spatial structures and physical properties of porous media. A 3D structure can be reconstructed from a single two-dimensional (2D) training image (TI) by using mathematical modeling methods. Among many reconstruction algorithms, an optimal-based algorithm was developed and has strong stability. However, this type of algorithm generally uses an autocorrelation function (which is unable to accurately describe the morphological features of porous media) as its objective function. This has negatively affected further research on porous media. To accurately reconstruct 3D porous media, a pattern density function is proposed in this paper, which is based on a random variable employed to characterize image patterns. In addition, the paper proposes an original optimal-based algorithm called the *pattern density function simulation*; this algorithm uses a pattern density function as its objective function, and adopts a multiple-grid system. Meanwhile, to address the key point of algorithm reconstruction speed, we propose the use of neighborhood statistics, the adjacent grid and reversed phase method, and a simplified temperature-controlled mechanism. The pattern density function is a high-order statistical function; thus, when all grids in the reconstruction results converge in the objective functions, the morphological features and statistical properties of the reconstruction results will be consistent with those of the TI. The experiments include 2D reconstruction using one artificial structure, and 3D reconstruction using battery materials and cores. Hierarchical simulated annealing and single normal equation simulation are employed as the comparison algorithms. The autocorrelation function, linear path function, and pore network model are used as the quantitative measures. Comprehensive tests show that 3D porous media can be reconstructed accurately from a single 2D training image by using the method proposed in this paper.

DOI: [10.1103/PhysRevE.93.012140](https://doi.org/10.1103/PhysRevE.93.012140)

### I. INTRODUCTION

Three-dimensional (3D) structures are useful for studying the microstructure of porous media. However, owing to a variety of factors, high-resolution 3D structures of porous media cannot be obtained directly or easily. On the other hand, computer technology and mathematical modeling methods can reconstruct 3D structures from a single high-resolution two-dimensional (2D) image under the 3D structures meeting with stationarity [1]. In recent years, numerous studies have been conducted to reconstruct complex 3D structures, and many classical algorithms have emerged. However, each of these algorithms has disadvantages in terms of meeting the demands of accurate reconstruction.

An accurate reconstruction algorithm should include the following three aspects. First, the statistical properties of the reconstructed result, such as porosity, the autocorrelation function, and linear path function, should be consistent with the training image (TI). Second, the morphological features of any slice of three orthogonal planes should be similar to those of the TI. Third, the algorithm should have strong stability, which refers to the ability to produce highly repeatable and comprehensive reconstructed results for different types of structures.

According to the reconstruction procedure, 3D reconstruction algorithms can be classified into two types: layer-by-layer reconstruction using 2D images, or reconstruction from 3D

space directly. In the former classification, the basic idea is to stack a series of 2D images to form a 3D structure. For this classification, typical algorithms include methods proposed by Tahmasebi and co-workers [2,3] and Hajizadeh and co-workers [4,5]. The key point of this classification is controlling the continuity and variability among adjacent layers. Gao *et al.* [6] proposed a three-step sampling algorithm that can effectively solve the problem. However, the reconstructed vertical morphological features are unsatisfactory and postprocessing is generally required [4,5], because patterns are only matched in the layer direction.

Optimal-based algorithms, such as simulated annealing [7–9], hierarchical simulated annealing (HSA) [10], and Gaussian random field [11–14], are the most typical algorithms of the latter classification. The objective function is set first, then the 3D structure is initialized according to the porosity of the TI; finally, points with different phases are selected and exchanged constantly until the reconstruction results gradually converge to the objective function. To avoid the local optimum in the iterative process, an annealing mechanism from a metal smelting process was introduced into the algorithm. Stability is the most significant advantage of this algorithm, which ensures that the reconstructed results will have the characteristics specified by the objective function when they converge to it. The key point of this algorithm is determining the objective function. Autocorrelation functions are generally used as the objective function in hierarchical simulated annealing. However, some works in the literature point out (and experiments show) that autocorrelation functions are unable to accurately describe the morphological features of complex

\*qzteng@scu.edu.cn

images, because images that meet with a single autocorrelation function may have vastly different morphologies.

The model proposed by Okabe and Blunt [15,16] is one typical method from the latter classification. To generate a 3D structure from a 2D image, statistics measured on the  $XY$  plane are transformed to the  $XZ$  and  $YZ$  planes with an assumption of isotropy in orthogonal directions. At every voxel to be assigned a pore or grain phase, three principal orthogonal planes intersecting the voxel ( $XY$ ,  $XZ$ , and  $YZ$ ) are used to locate conditioning data on these planes individually. The probability of the phase at each voxel on the different planes is estimated using single normal equation simulation (SNESIM). The three measured probabilities are then weighted by the amount of conditioning data on each plane to obtain a single probability for the voxel. Finally, to generate a 3D structure, the voxel phase is assigned based on this weighted probability. The result provides favorable connectivity; however, some key issues in this algorithm must be addressed: First, the criteria to determine the probability weights of the three vertical sections must be determined; second, the issue of SNESIM's instability in practical applications should be resolved [17–19].

Texture synthesis [20,21], a technique belonging to the latter classification, has developed rapidly in recent years. However, the reconstructed result only emphasizes visual similarity with the TI, while consciously ignoring the consistency of statistical properties.

Process-based reconstruction [22–26] also belongs to the latter classification. It still has certain limitations; for example, it requires substantial computer memory, and the required computations are very intensive. In addition, because they are based on actual physical processes, such models are not sufficiently general, as they were developed for specific types of porous media.

There have been other reconstruction algorithms, such as Markov random fields [27,28], fast frequency-domain transformation [29], discrete wavelet transformation algorithms [30,31], and neural network algorithms [32]; however, we will not discuss them here.

In order to reconstruct 3D porous media accurately, morphological features are used as the target of the reconstruction, and random variables are used to express the image patterns. The pattern density function is then proposed to express the distribution of probabilities for all patterns. Accordingly, pattern density function simulation (PDFSIM) is proposed. PDFSIM is an optimal-based algorithm that employs a multiple-grid system and uses a pattern density function as its objective function.

The pattern density function is a high-order statistical function; thus, when multiple-grid results converge in the objective function, it ensures that the morphological features of the reconstructed results will be similar to those of the TI, and implies that statistical property trends, including porosity, autocorrelation functions, and linear path functions, will be consistent with the TI.

Four measures were adopted to increase reconstruction speed. First, a relatively small template size ( $3\times 3$  pixels) was selected, based on the multiple-grid system. Second, the neighborhood statistics method was proposed to calculate the pattern density function of the 3D structure. Third, the adjacent grid and reversed phase method was adopted to

select the exchange points. Fourth, the temperature-controlled mechanism from the iterative process was simplified.

A 2D structure, battery materials, and core sample were used to test the proposed algorithm; the autocorrelation function, linear path function, and pore network model were used to quantize the reconstructed results. HSA and SNESIM were used to perform comparisons.

The remainder of the paper is organized as follows. The concepts behind the pattern density function are described in Sec. II. Section III presents the principles of PDFSIM. Section IV describes experimental results and analysis. The paper is summarized in Sec. V.

## II. PATTERN DENSITY FUNCTION

### A. Morphological features and patterns

Figure 1(a) shows a processed 2D slice selected from a 3D Micro-CT core sample. The white pixels indicate oil storage and are called the porous phase; black pixels indicate rock and are called the rock phase. The global and local shapes of an image are called morphological features. For example, area A (a  $25\times 25$  rectangle) represents the oil cavity, and area B (a  $17\times 17$  rectangle) represents the throat among the cavities. These morphological features determine permeability in oil extraction processes—thus, whether these morphological features can be reconstructed successfully and stably, which is a very important index to one reconstruction method.

The global morphological features of an image are combined with local morphological features. A local morphological feature is determined directly by the selection area, which is called a template. A template is composed of  $N\times N$  pixels;  $N$  is typically odd. The center of the  $N\times N$  area is called the template center. After setting the template center at the center of area B, a local morphological feature was extracted using the  $17\times 17$  template, as shown in Fig. 1(b). Figure 1(c) shows a local morphological feature extracted with the  $9\times 9$  template.

Figure 1(c) can be expressed as Fig. 2, in which one grid indicates one pixel. A local morphological feature extracted with a template is called a pattern. The entire image in Fig. 2 is a single pattern obtained using the  $9\times 9$  template. Any  $3\times 3$  area is a pattern that can be represented using a  $3\times 3$  template, such as the A and B areas marked with yellow rectangles. Therefore, a pattern is essentially a local morphological feature of an image, and is the best measure to express an image's morphological features [33]. Different

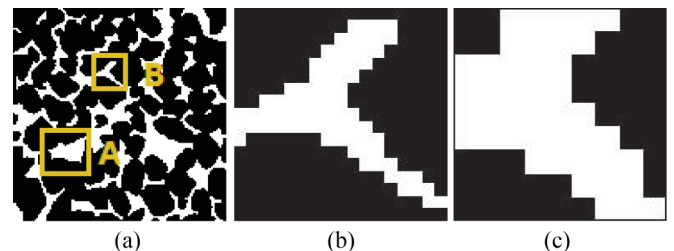


FIG. 1. Morphological features of an image. (a) The core image; (b) a local morphological feature extracted using the  $17\times 17$  template; (c) a local morphological feature extracted using the  $9\times 9$  template.

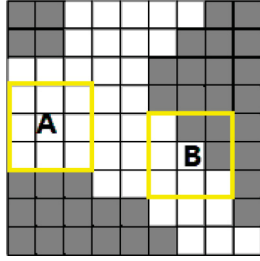


FIG. 2. Relationship between morphological feature and patterns.

patterns can be distinguished by coding, and all codes can constitute one variable,  $P$ .

### B. Multiple-grid system

Figures 1(b) and 1(c) show that the patterns extracted by the larger template can depict the morphological feature much more accurately. However, the number of patterns will increase sharply as the size of the template increases. For example, a template with a size of  $3 \times 3$  will extract  $2^{3 \times 3} = 512$  patterns, while  $2^{5 \times 5} = 335\,544\,32$  patterns can be extracted when a  $5 \times 5$  template is used. The sharp increase in patterns will cause a sharp increase in the number of calculations needed. This issue can be effectively resolved by using a multiple-grid system that enables small templates to obtain large morphological features [16,17]. For example, Figure 3 shows a three-grid system obtained using a  $3 \times 3$  template. This system includes sampling and reconstruction. The sampling process refers to the sequence from the first grid to the third grid, and the reconstruction process refers to the reverse sequence.

During reconstruction, the simulated data from the preceding grid will be used as conditional data for the following grid, in order to condition all corresponding areas in the following grids. Using the example in Fig. 3, the  $3 \times 3$  area in the third grid will condition the  $5 \times 5$  area in the second grid and the  $9 \times 9$  area in the first grid. Analyzing the patterns in Fig. 3 reveals that the  $3 \times 3$  template can control the morphological feature of a  $9 \times 9$  area by using three grids. More generally, for  $M$  grids, the area of size  $S_x^j \times S_y^j$  at grid  $j$  controlled by  $T_x \times T_y$  can be expressed as follows:

$$S_x^j \times S_y^j = [(T_x - 1)2^{M-j} + 1] \times [(T_y - 1)2^{M-j} + 1] \quad j = 1, 2, \dots, M. \quad (1)$$

To balance the speed and precision of the reconstruction process, a relatively small template ( $3 \times 3$ ) is adopted in this study. Thus, it must segment the TI into minimum size  $G_{\min}$  to

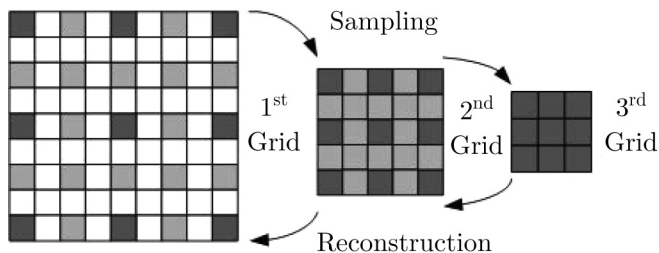


FIG. 3. Multiple-grid system.

obtain the morphological features effectively.  $G_{\min}$  represents a grid in which there are no  $3 \times 3$  regions belonging to a phase while the TI is segmented from the original size to a smaller one. This shows that all of the morphological features can be completely expressed by the  $3 \times 3$  template. Different images will be segmented into different series, and will usually exceed three grids. For example, the image shown in Fig. 1(a) will be segmented into four grids, so the  $17 \times 17$  area will be controlled nicely by the  $3 \times 3$  template, according to Eq. (1), and meanwhile the number of calculations will not be increased sharply. This shows that the morphological feature representing the throat [Fig. 1(b), size =  $17 \times 17$ ] will be depicted fully.

### C. Pattern density function

By scanning an entire image with a size of  $I_{\text{size}}$  using a specific template, we can obtain all patterns  $p_i$  ( $i = 1, 2, \dots, n_{\max}$ ) and corresponding numbers  $N_{p_i}$ . By using variable  $P$  to express all patterns and  $f(p_i)$  to express the probability of  $p_i$ ,  $f(p_i)$  can then be expressed in detail as follows:

$$f(p_i) = \begin{cases} \text{Prob}\{P = p_i\} = N_{p_i}/I_{\text{size}} \\ \sum_i \text{Prob}\{P = p_i\} = 1 & (i = 1, 2, \dots, n_{\max}). \\ n_{\max} = 2^{T_{\text{size}}^2} \end{cases} \quad (2)$$

$T_{\text{size}}$  is the template size, and  $n_{\max}$  is the maximum number of patterns.

According to the probability theory described in [34,35], Eq. (2) shows the distribution of probabilities for all patterns in one image, which can be referred to as the pattern density function. Figure 4(a) shows a processed battery materials image; Fig. 4(b) is the same as Fig. 1(a). The two images have visually different morphological features. Figure 4(c) also shows that the pattern density functions of the two images are obviously different; thus, pattern density functions can reflect the morphological features of a specific image. Note that a template with a size of only  $2 \times 2$  is used in Fig. 4(c). This smaller template was used to clarify the figure; the patterns would have bonded together if the  $3 \times 3$  template had been used.

For an  $M$  grids system, pattern density function can be expressed correspondingly as follows:

$$f(p_i^j) = \begin{cases} \text{Prob}\{P^j = p_i^j\} = N_{p_i^j}/I_{\text{size}}^j \\ \sum_i \text{Prob}\{P^j = p_i^j\} = 1 \\ n_{\max} = 2^{T_{\text{size}}^2} \end{cases} \quad (i = 1, 2, \dots, n_{\max}; j = 1, 2, \dots, M). \quad (3)$$

$I_{\text{size}}^j$  is the size of grid  $j$ , and  $N_{p_i^j}$  represents the number of pattern  $p_i^j$  of variable  $P^j$  in grid  $j$ . The pattern density function is equivalent to the joint pattern density function consisting of  $M$  variables; each variable has  $n_{\max}$  values.

Figures 5(a)–5(d) show four grids from Fig. 1(a); the pattern density functions are shown in Fig. 5(e). Different morphological features are depicted in different grids. Morphological features depicted in the larger grids (a and b) are the details of pores; the morphological features depicted in smaller grids (c and d) are the positions and contours of pores. Thus, during

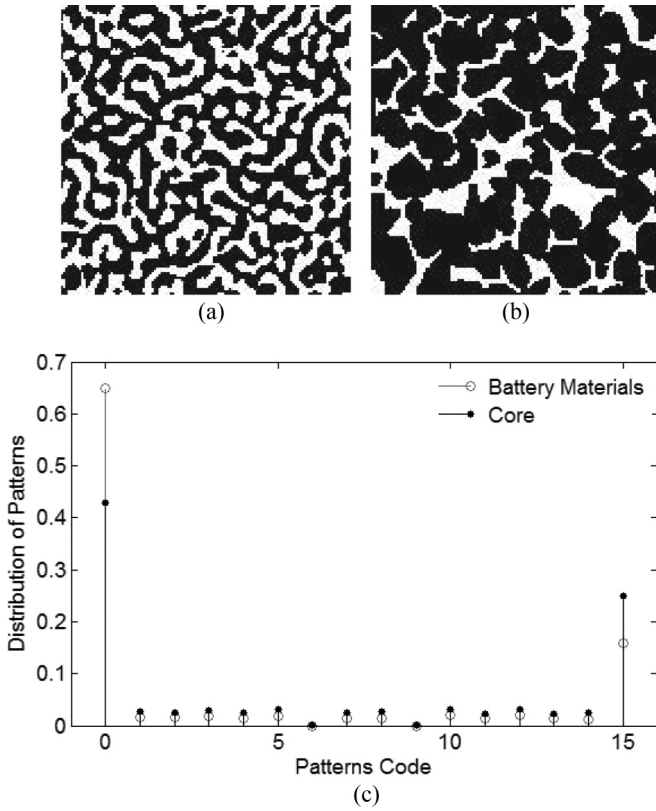


FIG. 4. Different images have different distributions of patterns. (a) Battery materials image with a size of  $128 \times 128$ ; (b) core image with a size of  $128 \times 128$ ; (c) distribution of patterns of the two images, using a  $2 \times 2$  template.

reconstruction, the positions and contours of the pores will be simulated first in smaller grids, and the details of the pores will be simulated later in larger grids. By considering the pattern density functions, it can be seen that when all grids in the reconstructed results tend to converge in the objective functions, which are the pattern density functions of the corresponding grids in the TI, the morphological features and statistical properties of the reconstruction results will be consistent with those in the TI.

### III. PRINCIPLES OF PDFSIM

Pattern density function simulation (PDFSIM) is a type of optimal-based algorithm, in which a pattern density function is used as the objective function and a multiple-grid system is adopted, and the reconstruction is an iterative process. After each exchange, the difference between the pattern density functions of the reconstructed results and the TI is calculated. The pattern density function is equivalent to the joint density function consisting of  $M$  variables when  $M$  grids are used, and each variable has  $2^{N \times N} = 512$  values when the template size is  $N \times N = 3 \times 3$ ; thus, convergence is very rigorous and speed is a very key point in PDFSIM. Neighborhood statistics, the adjacent grid and reversed phase method, and a simplified temperature-controlled mechanism are proposed to solve this problem.

#### A. Neighborhood statistical method

When using a 2D image to reconstruct the 3D structure, it is assumed that the 3D structure is isotropic [36–38]; thus,

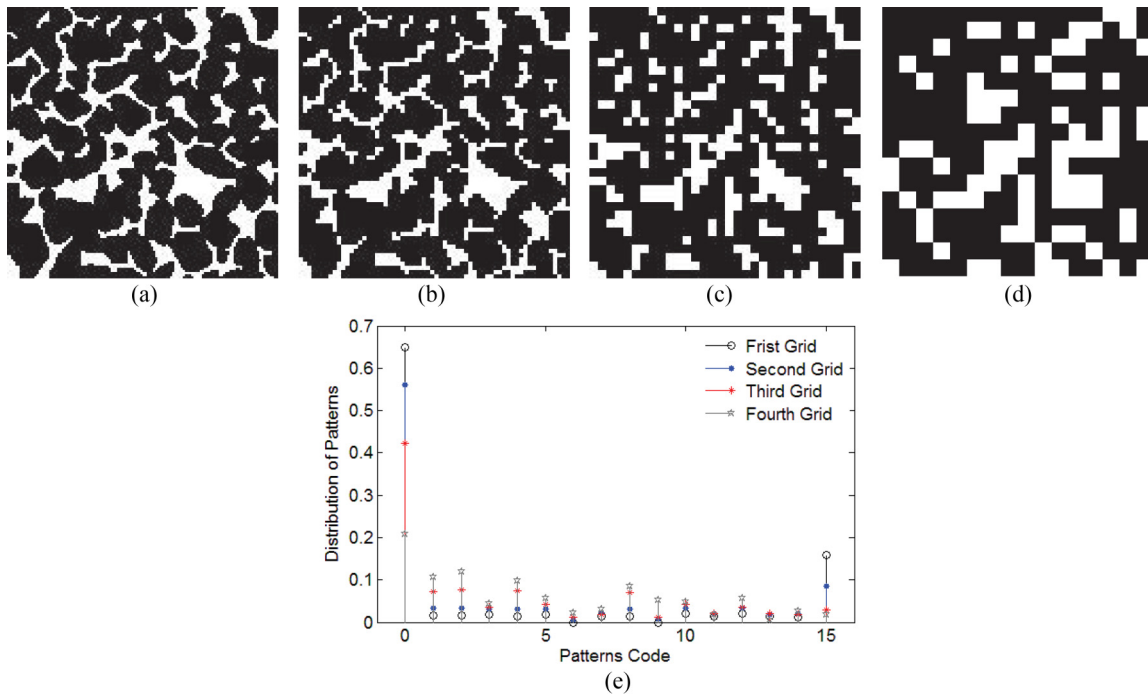


FIG. 5. PDFs of the multiple-grid system. (a) First grid, with a size of  $128 \times 128$ ; (b) second grid, with a size of  $64 \times 64$ ; (c) third grid, with a size of  $32 \times 32$ ; (d) fourth grid, with a size of  $16 \times 16$ ; (e) the pattern density functions of four grids, using a  $2 \times 2$  template.



FIG. 6. Eighteen changed patterns caused by two exchanged points, using a grid with a size of  $16 \times 16$ .

the morphological features of the three principal orthogonal planes can be represented by the 2D image. To reconstruct the 3D structure, the method must calculate the difference between the pattern density functions of the 2D image and the three vertical planes of the reconstruction structure, and assign the difference to the energy value  $E$ , as shown below:

$$E = \sum_p |f_{TI}(p) - f_{3D_x}(p)| + \sum_p |f_{TI}(p) - f_{3D_y}(p)| + \sum_p |f_{TI}(p) - f_{3D_z}(p)|. \quad (4)$$

$E$  indicates the difference between the reconstructed result and TI; a lower  $E$  value indicates a smaller difference. Considering an example with a  $128 \times 128$  image and the  $3 \times 3$  template, one grid requires  $128 \times 128 \times 3 \times 3$  iterations to calculate the pattern density function of the reconstruction image only once by counting the patterns of the entire image; 512 iterations are then required to calculate  $E$  and transmit the pattern density function. Typically, millions of iterations are required to reconstruct one image, which makes PDFSIM unsuitable in practice.

Fortunately, the largest number of changed patterns that are caused by point exchanges for two  $3 \times 3$  neighborhoods is 18, as shown in Fig. 6. After the two points are exchanged, the white and black centers of the unchanged patterns are assigned pixel values of 255 and 0, respectively; the white and black centers of changed patterns are assigned pixel values of 170 and 85, respectively. Only the changed value of  $E$  must be calculated; this requires  $18 \times 3 \times 3$  iterations to count the pattern density functions, 18 iterations to calculate the value of  $E$ , and 18

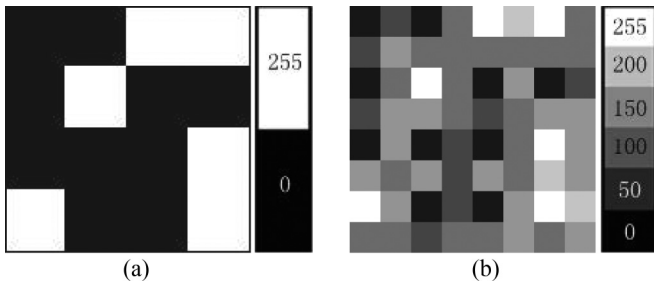


FIG. 7. Schematic of adjacent grid and reversed phase method: (a)  $4 \times 4$  grid; (b)  $8 \times 8$  grid expanded by (a) and added points.

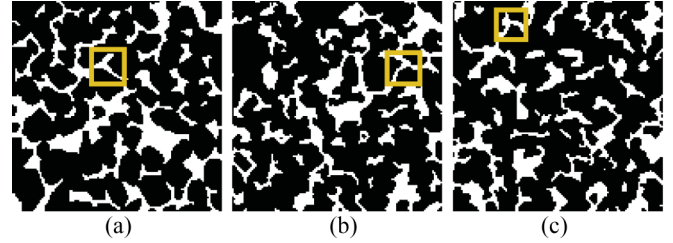


FIG. 8. The results of core image reconstructed by temperature-controlled mechanism and simplified temperature-controlled mechanism, respectively. (a) Core sample; (b) the result reconstructed by temperature-controlled mechanism; (c) the result reconstructed by simplified temperature-controlled mechanism.

iterations to transmit the pattern density functions. Hence, the neighborhood statistical method can shorten the reconstruction process by dozens of iterations and make PDFSIM usable for reconstruction.  $D$  represents the changed neighborhood; energy  $E$  can be expressed as follows:

$$E = \sum_{p \in D_x} |f_{TI}(p) - f_{3D_x}(p)| + \sum_{p \in D_y} |f_{TI}(p) - f_{3D_y}(p)| + \sum_{p \in D_z} |f_{TI}(p) - f_{3D_z}(p)|. \quad (5)$$

**B. Adjacent grid and reversed phase method (AGRPM)**

The adjacent grid and reversed phase method is used to select the exchange points, and is proposed based on two considerations. First, with iterative deepening, the pores will tend to aggregate. Second, in a multiple-grid system, the simulated points on the former grid are used as the conditional data on the current grid; this largely determines the value of the surrounding points.

First, the point that is simulated on the former grid is set as the center point of the neighborhood (a  $3 \times 3$  domain in a 2D structure, or a  $3 \times 3 \times 3$  domain in a 3D structure) of the current grid. If the center point is white, the black points randomly arranged on the current grid are selected as the exchange points belonging to this neighborhood; accordingly, if the center point is black, the white points are selected as the exchange points.

The method is shown in Fig. 7. Grid (b) with a size of  $8 \times 8$  is expanded by grid (a) with a size of  $4 \times 4$ . The simulated white and black points in grid (a) are assigned pixel values of 255 and 0, respectively. The white and black points selected for exchanging on grid (b) are assigned pixel values of 150 and 100, respectively. The white and black points not selected for exchanging on grid (b) are assigned pixels values of

TABLE I. The remnants  $E$  of the results reconstructed by PDFSIM TM and PDFSIM STM.

	Remnants $E$			
	First grid	Second grid	Third grid	Fourth grid
PDFSIM TM	0.5%	1.7%	4.6%	6.4%
PDFSIM STM	0.6%	1.9%	4.7%	6.3%

TABLE II. The time cost of the results reconstructed by different methods.

	Times (s)
PDFSIM TM	56
PDFSIM STM	15
HSA	20
SNESIM	20

200 and 50, respectively. The periodic boundary condition is considered. Only 36 points are selected from the 48 added random points by using this method. With iterative deepening, the number of points that can be selected as exchange points decreases constantly as the polymerization and speed of convergence rapidly accelerate. Experiments prove that this method can significantly improve reconstruction speed.

### C. Simplified temperature-controlled mechanism

After each exchange, it is necessary to calculate the changed energy  $\Delta E$ , which is the value used for accepting the new state.  $E_{OR}$  and  $E$  indicate the energy before and after exchanging, respectively;  $\Delta E$  can be expressed as follows.

$$\Delta E = E_{OR} - E. \quad (6)$$

In order to prevent the local optimum in the iterative operation, the HSA introduces the temperature-controlled mechanism (TM), which is the Metropolis criterion [7,8]:

$$p(\Delta E) = \begin{cases} 1, & \Delta E \leq 0 \\ \exp(-\Delta E/T), & \Delta E > 0 \end{cases}. \quad (7)$$

$T$  indicates the current temperature of the reconstruction structure. However, the temperature-controlled mechanism greatly decelerates the iteration. To accelerate the iterative procedure, a type of simplified temperature-controlled mechanism (STM) is adopted in this study, in which a temperature-controlled mechanism is only used at the minimum grid and the remaining grids are not considered. Thus, the acceptance

criterion of the remaining grids can be expressed as follows:

$$p(\Delta E) = \begin{cases} 1, & \Delta E \leq 0 \\ 0, & \Delta E > 0 \end{cases}. \quad (8)$$

Two reasons can support this view. First, the experiments indicate that local optimization can easily occur in the minimum grid. Second, the simulated points on the former grid, which are arranged as the conditional data on the current grid, can prevent local optimization effectively. Figure 8 shows the results reconstructed by the PDFSIM based on temperature-controlled mechanism (PDFSIM TM) and simplified temperature-controlled mechanism (PDFSIM STM), respectively. Tables I and II show the remnants of  $E$  and the time cost of the two methods. A 3.4 GHz Intel machine was used in these experiments. The experimental results show that the simplified temperature-controlled mechanism can greatly increase reconstruction speed and does not significantly affect reconstruction of the random structure. Meanwhile, the two methods can accurately reconstruct the morphological features of the throat, which are marked with yellow rectangles in Figure 1(a).

### D. 3D reconstruction procedure

Before reconstruction, the TI should be segmented into multiple grids and two calculations must be performed. First, the pattern density function of every TI grid is calculated and then assigned as the objective function of the corresponding reconstruction grid. Second, the porosity of every TI grid is calculated, and then used as the objective porosity of the reconstruction grid.

The reconstruction begins with the smallest grid, in which all data are arranged randomly according to the objective porosity. Two points with different phases are randomly selected, and the difference between the pattern density functions of the reconstruction grid and TI grid is calculated according to formulas (5) and (6). The exchange state will then be accepted according to formula (7). Using continuous

TABLE III. The procedure of PDFSIM.

(1)	Calculate the min grid $G_{\min}$ and the max grid $G_{\max}$ ;
(2)	for ( $G = G_{\min}$ ; $G! = G_{\max}$ ; $G++$ )
(3)	Initialize the grid $G$ , treated differently according to the $G_{\min}$ and others;
(4)	Set the energy limit $E_G$ to exit cycle.
(5)	Calculate the energy $E$ of the reconstructing 3D structure;
(6)	while ( $E > E_G$ )
(7)	Select the exchanging points sets $set_w$ and $set_b$ according to AGRPM;
(8)	Set loop times $T_i = \min(S_w, S_b)$ ;
(9)	for ( $T = T_i$ ; $T! = 0$ ; $T--$ )
(10)	Select the exchanging points $p_w$ and $p_b$ randomly from $set_w$ and $set_b$ , respectively.
(11)	Calculate the changed energy $\Delta E$ according to neighborhood statistical method.
(12)	if ( $\Delta E < 0$ )
(13)	Exchange the points $p_w$ and $p_b$ , and preserve the new pattern density function;
(14)	else
(15)	Cancel the exchanged points $p_w$ and $p_b$ , and recover the pattern density function.
(16)	End 9.
(17)	End 2.
(18)	The 3D structure is produced and the procedure is finished.

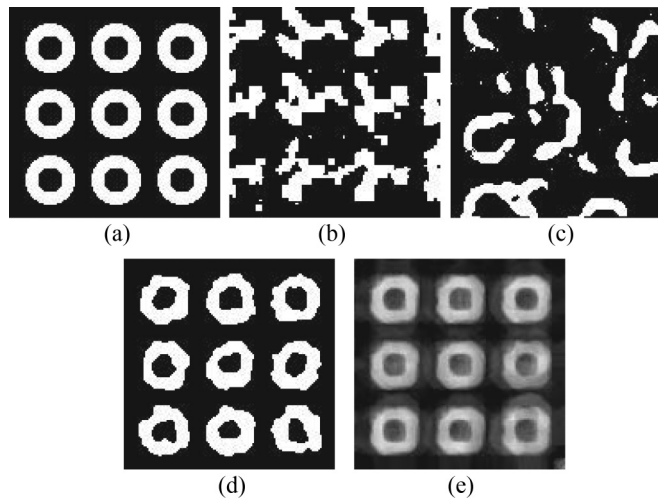


FIG. 9. The results of a 2D artificial image reconstructed by different methods. (a) Original image; (b) the result reconstructed by HSA; (c) the result reconstructed by SNESIM; (d) the result reconstructed by PDFSIM; (e) an E-type image composed by 90 results reconstructed by PDFSIM.

iteration, the pattern density function of the reconstruction grid will gradually converge in the objective function. When the grid is simulated, all data will be arranged at the corresponding location in the next grid and set as the conditional data. All operations are the same as before, except for the accepting condition defined in formula (8). When the iteration exits from the largest grid, the entire reconstruction process is complete. Additional details about the algorithm are shown in Table III.

## IV. RESULTS AND DISCUSSION

### A. 2D reconstruction

In order to display the results reconstructed by PDFSIM, an artificial structure consisting of concentric rings was selected to represent a certain complex structure, as shown in Fig. 9(a). The results produced by HSA and SNESIM are provided for comparison. SNESIM used a template size of  $9 \times 9$ ; its minimum number of repetitions was five. The conditions used by HSA and PDFSIM specified an acceptance probability of 0.5 in the first exchange; this probability was used to set the initial temperature. They also specified that the temperature would decrease by 1%.

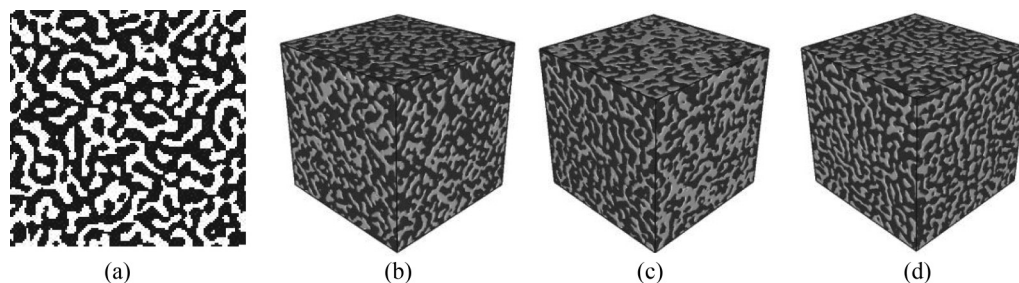


FIG. 10. Three-dimensional reconstructed results of the battery material. (a) Two-dimensional training image; (b) the result reconstructed by HSA; (c) the result reconstructed by SNESIM; (d) the result reconstructed by PDFSIM.

Comparing the results in Figs. 9(b)–9(d), which were reconstructed by HSA, SNESIM, and PDFSIM, respectively, it is clear that PDFSIM can reconstruct morphology more accurately than the other solutions. Figure 9(e) is an E-type image composed of 90 results reconstructed by PDFSIM; this image can be used to indicate the stability of an algorithm. The E-type image can reproduce the TI clearly, which indicates that PDFSIM has strong stability.

### B. 3D reconstruction using a 2D image of battery material

Figure 10(a) shows a processed microstructure image of the compound  $\text{NiO-CeO}_2$  (which is commonly used as battery material) under  $1250^\circ\text{C}$ ; the image has a resolution of  $10\ \mu\text{m}$ . Figures 10(b)–10(d) show the 3D results reconstructed by HAS, SNESIM, and PDFSIM, respectively. The reconstructing conditions are consistent with 2D reconstruction.

In order to display the morphological features of the 3D structure's three orthogonal planes, the 2D slices of the  $XY$ ,  $XZ$ , and  $YZ$  planes of the 3D reconstructed results are shown in Fig. 11 for comparison. Experiments show that the morphological features of the  $XY$ ,  $XZ$ , and  $YZ$  planes from the 3D results reconstructed by HSA, such as those shown in (a)–(c), are consistent but not ideal. The  $XY$  plane of the 3D results reconstructed by SNESIM, which is based on the layer-by-layer method, can reproduce morphological features such as (d) accurately. However, because it uses an asymmetric process, the morphological features of the  $XZ$  and  $YZ$  planes are insufficient; examples are shown in (e) and (f). The morphological features of all three planes can be reconstructed accurately by PDFSIM, as shown in (h)–(j).

In order to quantify the morphological difference between the TI and the results reconstructed by the different methods, Table IV shows the differences between the pattern density functions of the TI and the methods' reconstruction results for three orthogonal planes in three grids. To differentiate the reconstruction, the  $5 \times 5$  template is used here. The statistics data in the table also indicate that the morphological features of PDFSIM's reconstruction results show the highest similarity to the TI, and that the morphological features of the three orthogonal planes are consistent.

### C. 3D reconstruction using a 2D image of core

In this section, one 3D Micro-CT core sample, with a size of  $128 \times 128 \times 128$  pixels and a resolution of  $10\ \mu\text{m}$ , is used for further testing. The sample does not exhibit much variability.

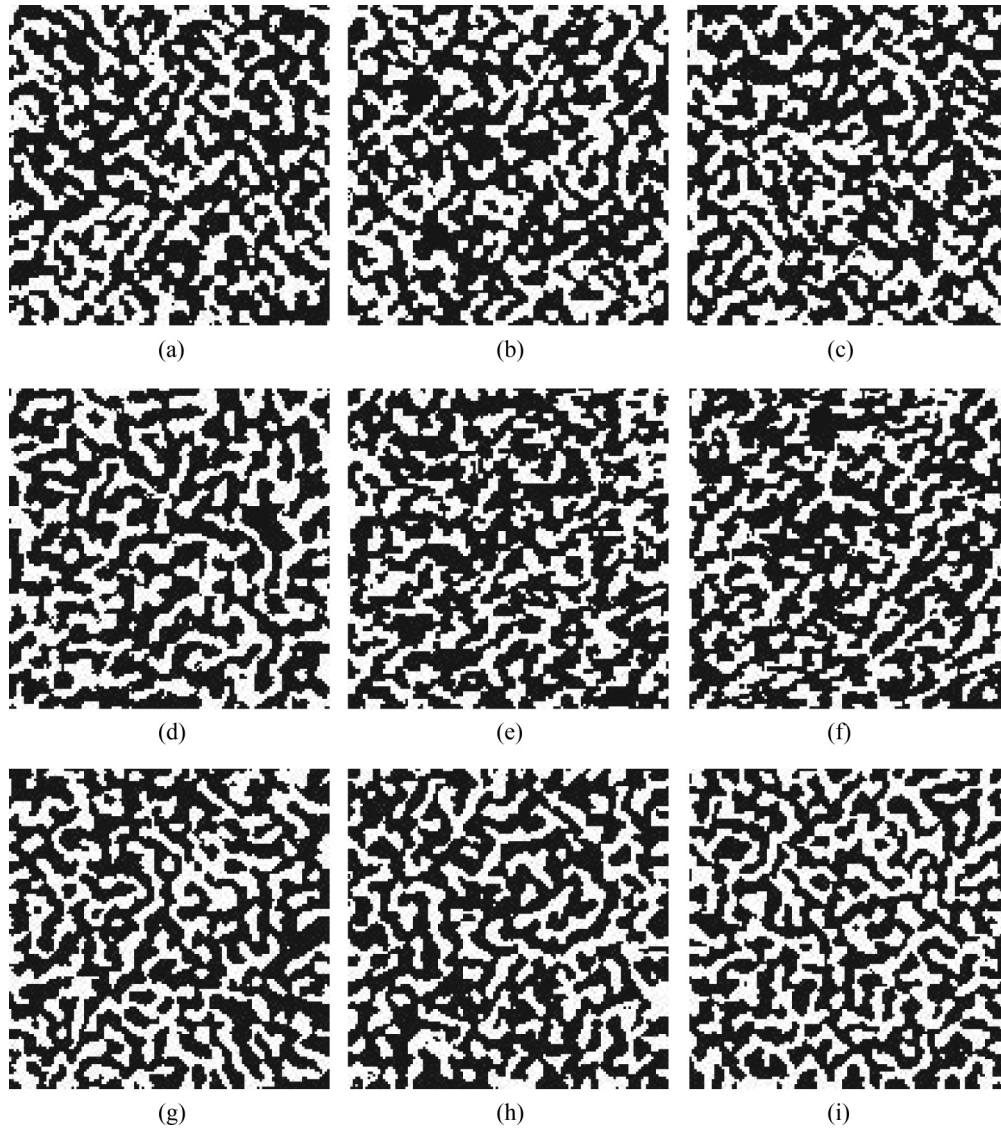


FIG. 11. Morphological features of three orthogonal planes of 3D reconstructed results. (a–c) The slices of XY, XZ, and YZ planes of the 3D result reconstructed by HSA; (d–f) the slices of XY, XZ, and YZ planes of the 3D result reconstructed by SNESIM; (g–i) the slices of XY, XZ, and YZ planes of the 3D result reconstructed by PDFSIM.

One 2D image from this 3D sample is selected as the TI, as shown in Fig. 12(a). It has a porosity of 0.252, consistent with the porosity of 0.246 in the 3D sample. The 2D image

TABLE IV. The morphological difference between TI and reconstructed results.

		First grid	Second grid	Third grid
HSA	XY plane	12.1%	18.5%	21.7%
	XZ plane	13.6%	17.5%	22.3%
	YZ plane	12.2%	17.1%	22.5%
SNESIM	XY plane	3.6%	7.1%	8.8%
	XZ plane	13.2%	24.1%	31.4%
	YZ plane	14.3%	24.4%	30.1%
PDFSIM	XY plane	2.2%	3.7%	7.3%
	XZ plane	2.2%	3.6%	6.0%
	YZ plane	1.8%	3.5%	6.4%

has the typical morphological features of the 3D sample, and its low-order statistics characteristics are consistent with the 3D sample. The reference Micro-CT samples are shown in (b) and (c), and the reconstructed results are shown in (d) and (e). By observing its appearance, it is evident that the morphological features of the reconstructed 3D result exhibit perfect similarity with the Micro-CT sample.

The autocorrelation function and linear path function were selected to further quantify the reconstructed result. The void-void (pore-pore) autocorrelation function is defined by

$$R(r) = \frac{\langle [I(u) - \phi][I(u+r) - \phi] \rangle}{\phi - \phi^2}, \quad (9)$$

where the averaging is over all locations  $u$  within the volume, and  $I(u)$  is an indicator function such that  $I(u) = 1$  if  $r$  is in the pore space, and  $I(u) = 0$  otherwise. The porosity is simply  $\phi = \langle I(u) \rangle$ . The comparisons between the autocorrelation

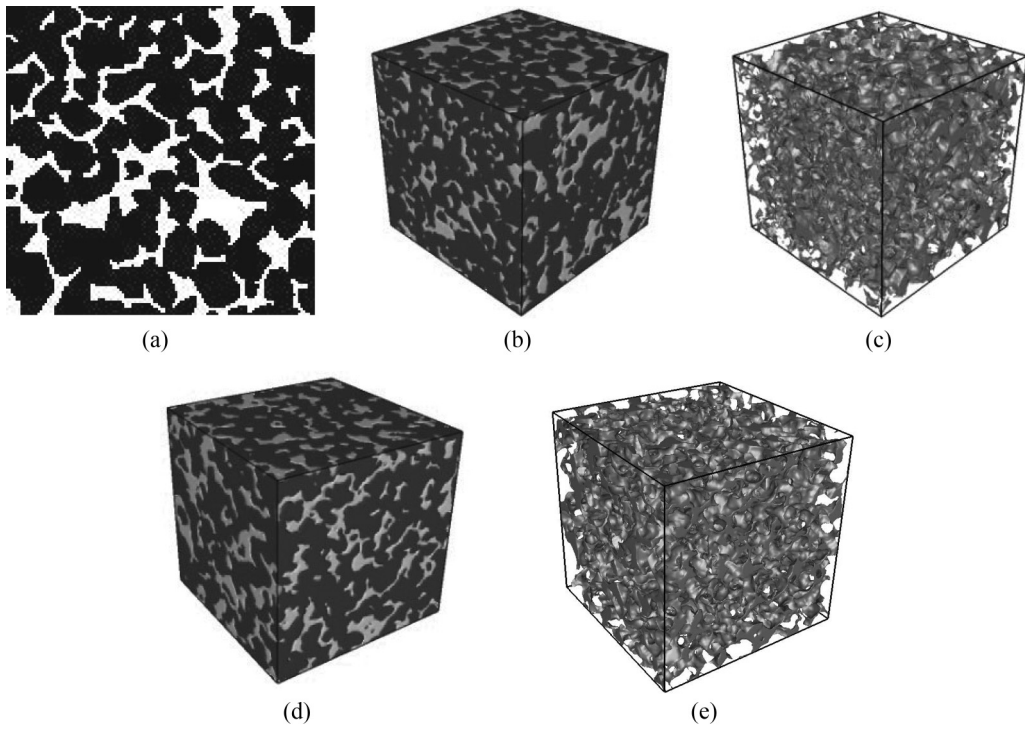


FIG. 12. Three-dimensional reconstructed results of the core. (a) Two-dimensional training image; (b) 3D structure of Micro-CT sample; (c) the perspective image of Micro-CT sample; (d) reconstructed result; (e) the perspective image of reconstructed result.

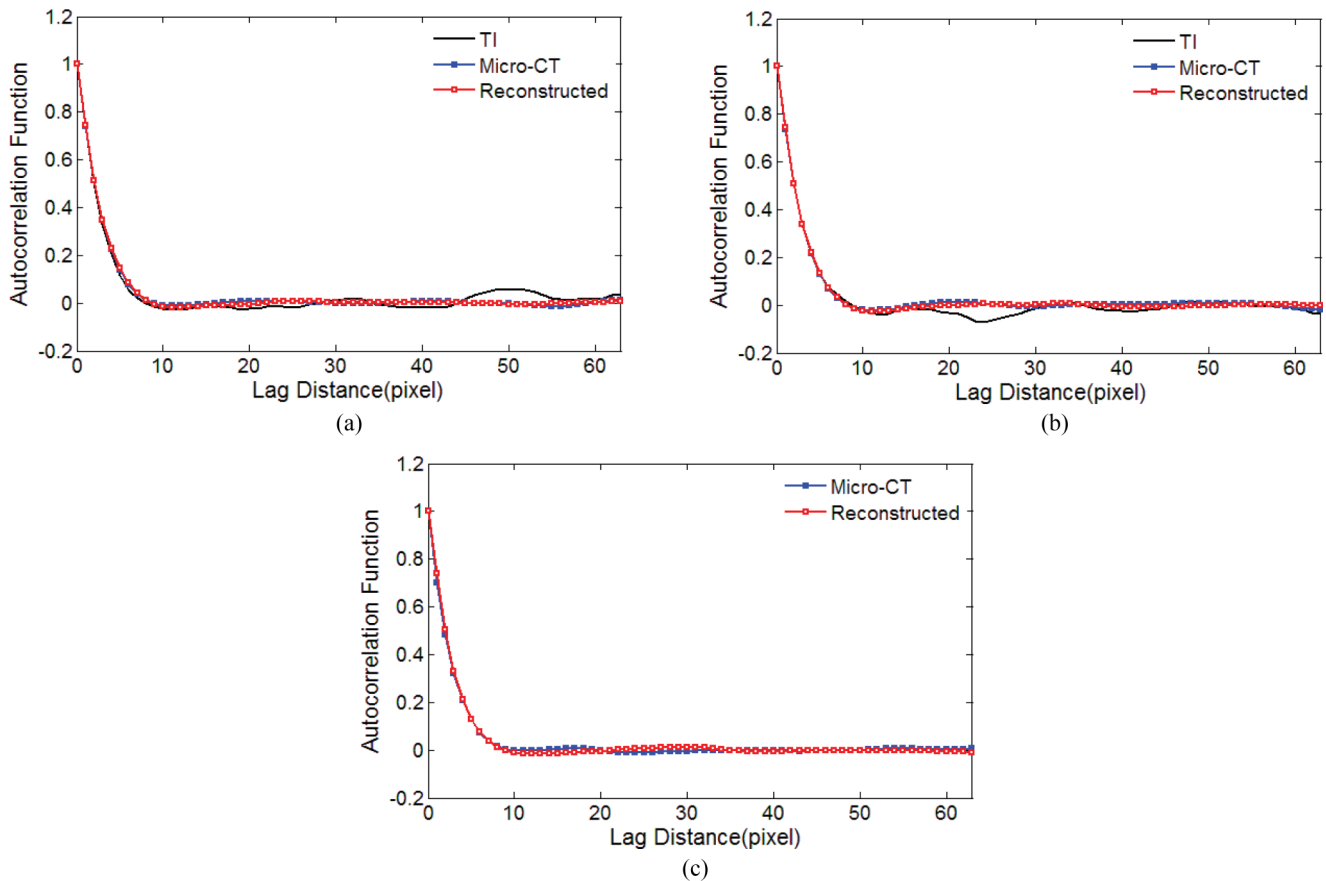


FIG. 13. Comparison of autocorrelation functions, in (a) the  $x$  direction, (b) the  $y$  direction, and (c) the  $z$  direction.

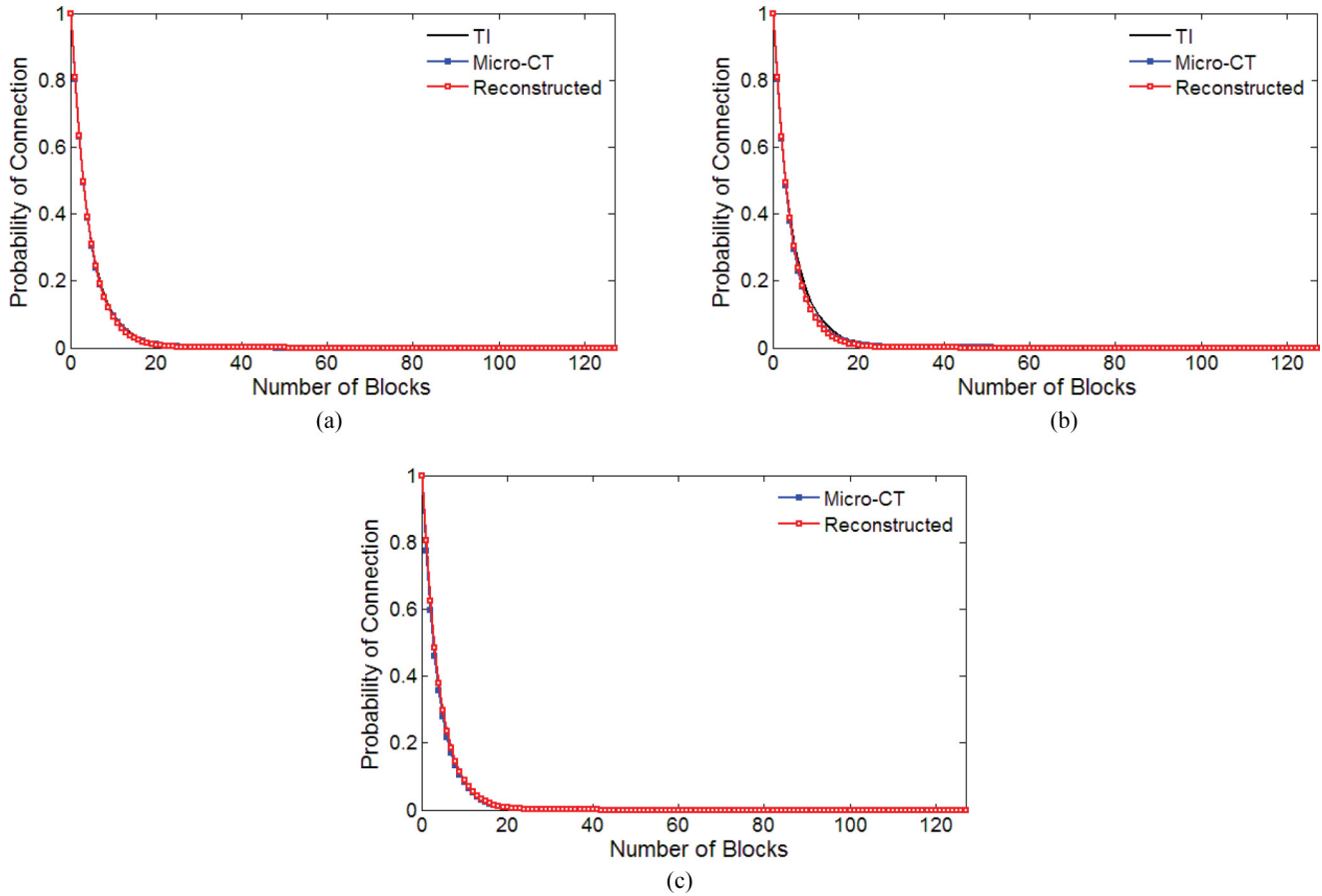


FIG. 14. Comparison of linear path functions, in (a) the  $x$  direction, (b) the  $y$  direction, and (c) the  $z$  direction.

functions of Micro-CT and the reconstructed results are shown in Fig. 13.

The linear path function, also called the multiple-points connectivity probability, characterizes the local connectivity of the pores. This quantity is the probability that a line segment  $l_r$  of length  $r$  is entirely in pore space. In practice, the probability is estimated only along three orthogonal directions of a 3D structure. The normalized linear path function can be defined by

$$L(r) = \frac{\text{Prob}\{I(u) = 1, I(u+1) = 1, \dots, I(u+r) = 1\}}{\phi}, \quad (10)$$

where  $u$  is the outset of the line segment  $l_r$ ,  $I(u)$  is an indicator function such that  $I(u) = 1$  if  $u$  is in the pore space, and  $I(u) = 0$  otherwise. The porosity is  $\phi = L(0)$ . The comparisons between the lineal path functions of Micro-CT and the reconstructed results are shown in Fig. 14.

Figures 13 and 14 show that the low-order statistics properties of the reconstructed results are very consistent with the related samples, although PDFSIM does not use these functions as the reconstructing condition. As mentioned previously, this occurs because the pattern density function is a high-order statistical function, which implies these low-order statistical functions.

To comprehensively test the spatial characteristics and relative permeability for the two-phase flow of the reconstructed 3D results, we used the pore-throat networks model

proposed by Dong and Blunt [39], who used the maximal ball algorithm to extract the sizes of the pores and throats from the structure of a porous medium. This algorithm was developed to extract topologically disordered networks of pores and throats with parametrized geometry and interconnectivity, shown as Fig. 15. Table V compares some important parameters of the pores and throats in the pore network model from the Micro-CT sample of carbonate rock and 20 continuous reconstructed results. The two sets of results agree well—almost all parameters of the reconstructed porous media are in accordance with the Micro-CT of the porous media. In

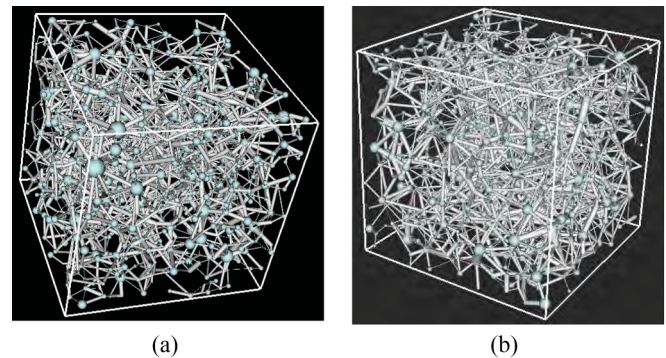


FIG. 15. Pore-throat network model. (a) The pore-throat network model of Micro-CT; (b) the pore-throat network model of reconstructed result.

TABLE V. Some important parameters of the pore and throat in the pore network.

	Micro-CT	Mean	Proportion of standard deviation
Number of pores	1132	1232	1.1%
Number of throats	3207	3234	0.9%
Shape factor	0.030	0.030	0.0%
Size of pore radius (m)	$1.68 \times 10^{-5}$	$1.67 \times 10^{-5}$	0.6%
Size of throat radius (m)	$7.45 \times 10^{-6}$	$7.32 \times 10^{-6}$	0.7%
Volume of pore (m <sup>3</sup> )	$3.88 \times 10^{-13}$	$3.70 \times 10^{-13}$	1.3%
Volume of throat (m <sup>3</sup> )	$2.33 \times 10^{-14}$	$2.25 \times 10^{-14}$	2.2%
Radius size ratio of pore and throat	0.308	0.308	1.2%
Coordination number	5.668	5.25	7.1%
Effective permeability (mD)	1570	1275	6.2%

particular, the shape factor of the reconstructed result, which indicates the rate of the area and the perimeter of the pores slice [40], is equal to that of Micro-CT at every instance. Furthermore, the reconstructed results exhibit strong stability.

The two-phase flow test included a two-step procedure. During the primary flooding, the pore network is assumed to be strongly wetted by the wetting phase (by water in water-oil systems, oil in oil-gas systems, or oil in the carbonate rock), with a receding contact angle of 0° and an advancing contact angle of 0°. During the secondary flooding, the receding contact angle was set to 50° and the advancing contact angle was set to 60°. The oil and water densities were assumed to be 900 and 1000 kg/m<sup>3</sup>, respectively, and the water-oil surface tension was assumed to be  $3 \times 10^2$  N/m; the oil and water viscosities were assumed to be  $1.05 \times 10^3$  and  $1.0 \times 10^3$  kg/(m s), respectively. The computed results for both the reconstructed result and the Micro-CT sample are presented in Fig. 16. The agreement between the two 3D structures is excellent. This provides strong evidence that the reconstructed result has a very similar microstructure to that of Micro-CT.

Comprehensive experiments show that the method proposed in this paper can accurately reconstruct complex 3D structures of porous media from a single 2D training image.

V. CONCLUSION

To accurately reconstruct the morphological features of 3D porous media using a single 2D training image, the pattern

density function and pattern density function simulation are proposed in this paper. Further, to increase the algorithm’s reconstructing speed, neighborhood statistics, the adjacent grid and reversed phase method, and a simplified temperature-controlled mechanism are also proposed.

Three sets of experiments were used to comprehensively test the proposed algorithm. In the first set of experiments, one artificial structure was processed using 2D reconstruction to facilitate a direct visual comparison. In the second set of experiments, a 2D image of a type of battery material was used to reconstruct a 3D structure, which shows the same effect as the three orthogonal planes of a 3D reconstructed result. A Micro-CT core sample was used in the third experiment. Additional measures, including the autocorrelation function, linear path function, and the pore network model, were used to qualify the reconstruction results. Comprehensive tests show that morphological features of a TI can be reconstructed accurately, and that the low-order statistics of the reconstructed results are perfectly consistent with the TI; moreover, the algorithm has strong stability.

Several experiments demonstrate that the algorithm proposed in this paper performs well when the 2D training image is a sample of a stationary random 3D structure. While the 2D training image is restricted to a limited domain and the morphological features of the 3D structure cannot be obtained thoroughly, the reconstructed results are unsatisfactory. Besides, a small size template (3×3 pixels) is used in this paper considering the reconstruction speed, but to precisely describe

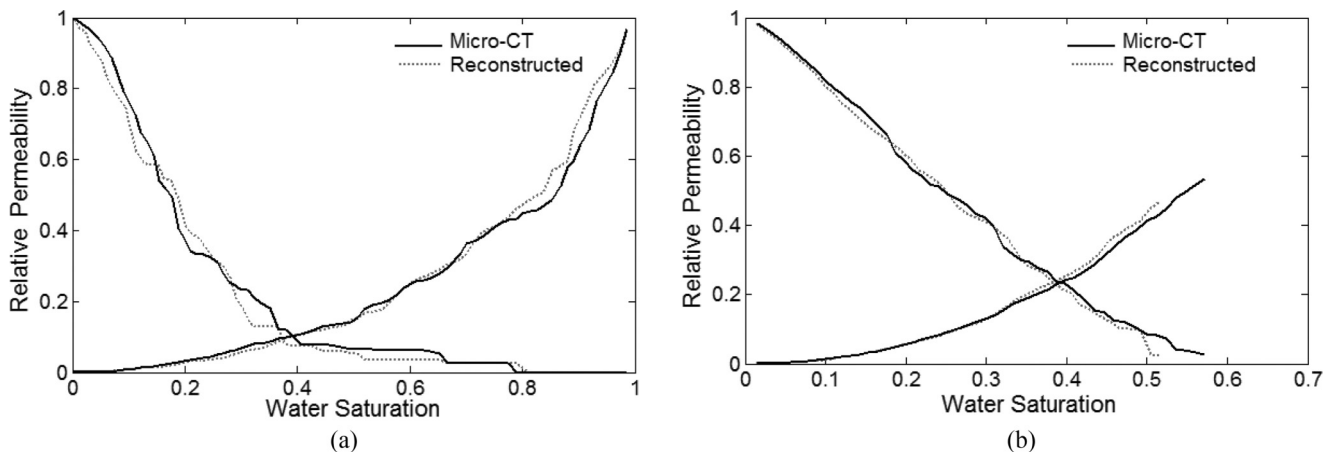


FIG. 16. Relative permeability curves of the 3D micro-CT image and the 3D reconstructed result. (a) Drainage and (b) imbibition.

the morphological features with much larger size a larger template is needed.

Considering its accuracy, we believe that the algorithm proposed in this paper can be used for practical applications. The method also has potential applications in the reconstruction of a wide variety of anisotropic systems, some of which will be studied and reported on in the near future. Improving

the algorithm's reconstruction speed will also require further research.

#### ACKNOWLEDGMENT

This work was supported by the National Natural Science Foundation of China (Grant No. 61372174).

- 
- [1] X. Emery and C. Lantuejoul, *Math Geosci.* **46**, 133 (2014).
- [2] P. Tahmasebi and M. Sahimi, *Phys. Rev. E* **85**, 066709 (2012).
- [3] P. Tahmasebi, A. Hezarkhani, and M. Sahimi, *Comput. Geosci.* **16**, 779 (2012).
- [4] A. Hajizadeh, A. Safekordi, and F. A. Farhadpour, *Adv. Water Resour.* **34**, 1256 (2011).
- [5] A. Hajizadeh and Z. Farhadpour, *Transp. Porous Media* **94**, 859 (2012).
- [6] M. L. Gao, X. H. He, Q. Z. Teng, C. Zuo, and D. D. Chen, *Phys. Rev. E* **91**, 013308 (2015).
- [7] C. L. Y. Yeong and S. Torquato, *Phys. Rev. E* **57**, 495 (1998).
- [8] C. L. Y. Yeong and S. Torquato, *Phys. Rev. E* **58**, 224 (1998).
- [9] D. D. Chen, X. H. He, Q. Z. Teng, Z. Xu, and Z. J. Li, *Phys. A (Amsterdam, Neth.)* **415**, 240 (2014).
- [10] D. D. Chen, Q. Z. Teng, X. H. He, Z. Xu, and Z. J. Li, *Phys. Rev. E* **89**, 013305 (2014).
- [11] J. A. Quiblier, *J. Colloid Interface Sci.* **98**, 84 (1984).
- [12] P. M. Adler, C. G. Jacquin, and J. A. Quiblier, *Int. J. Multiphase Flow* **16**, 691 (1990).
- [13] Z. Jiang, W. Chen, and C. Burkhart, *J. Microsc.* **252**, 135 (2013).
- [14] J. Feinauer, T. Brereton, A. Spettil, M. Weber, I. Manke, and V. Schmidt, *Comput. Mater. Sci.* **109**, 137 (2015).
- [15] H. Okabe and M. J. Blunt, *Phys. Rev. E* **70**, 066135 (2004).
- [16] H. Okabe and M. J. Blunt, *J. Pet. Sci. Eng.* **46**, 121 (2005).
- [17] S. Strebelle and C. Claude, *Math. Geosci.* **46**, 171 (2013).
- [18] S. Strebelle, *Math. Geol.* **34**, 1 (2002).
- [19] S. Strebelle, Ph.D. thesis, Stanford University, 2000.
- [20] A. Parra and J. M. Ortiz, in Proceedings of the IAMG 2009 Conference, Stanford University, 2009 (unpublished).
- [21] A. Parra and J. M. Ortiz, *Stochastic Environ. Res. Risk Assess.* **25**, 1101 (2011).
- [22] J. N. Roberts and L. M. Schwartz, *Phys. Rev. B* **31**, 5990 (1985).
- [23] L. M. Schwartz and S. Kimminau, *Geophysics* **52**, 1402 (1987).
- [24] S. L. Bryant and M. J. Blunt, *Phys. Rev. A* **46**, 2004 (1992).
- [25] S. L. Bryant and S. Raikes, *Geophysics* **60**, 437 (1995).
- [26] J. P. Latham, A. Munjiza, and Y. Lu, *Powder Technol.* **125**, 10 (2002).
- [27] S. Theodoridis, and K. Koutroumbas, *Pattern Recognition and MATLAB Intro: Pattern Recognition* (Academic Press, New York, 2007).
- [28] C. Daly, *Higher Order Models Using Entropy, Markov Random Fields and Sequential Simulation* (Springer Netherlands Press, Dordrecht, 2005).
- [29] L. Borgman, M. Taheri, and R. Hagan, *Three-dimensional, Frequency-domain Simulations of Geological Variables* (Springer Netherlands Press, Dordrecht, 1984).
- [30] E. Gloaguen and R. Dimitrakopoulos, *Math. Geosci.* **41**, 679 (2009).
- [31] M. Sahimi, *Comput. Sci. Eng.* **5**, 75 (2003).
- [32] J. Caers, S. Srinivasan, and A.G. Journel, *SPE Reservoir Eval. Eng.* **3**, 457 (2000).
- [33] R. C. Gonzalez and R. E. Woods, *Digital Image Processing*, 2nd ed. (Pearson Education Press, New York, 2002).
- [34] S. Karlin and H. M. Taylor, *A First Course in Stochastic Processes*, 2nd ed. (Elsevier, Amsterdam, 1975).
- [35] A. Papoulis and S. U. Pillai, *Probability, Random Variables and Stochastic Processes* (McGraw-Hill Press, New York, 2002).
- [36] H. Hamzehpour and M. Sahimi, *Phys. Rev. E* **74**, 026308 (2006).
- [37] Y. Jiao, F. H. Stillinger, and S. Torquato, *Proc. Natl. Acad. Sci. USA* **106**, 17634 (2009).
- [38] C. E. Zachary and S. Torquato, *Phys. Rev. E* **84**, 056102 (2011).
- [39] H. Dong and M. J. Blunt, *Phys. Rev. E* **80**, 036307 (2009).
- [40] G. Mason and N. R. Morrow, *J. Colloid Interface Sci.* **141**, 262 (1991).